

Fermi Velocity Dependent Critical Current in Ballistic Bilayer Graphene Josephson Junctions

Amis Sharma,[†] Chun-Chia Chen,[‡] Jordan McCourt,[‡] Mingi Kim,[¶] Kenji Watanabe,[§] Takashi Taniguchi,[§] Leonid Rokhinson,[¶] Gleb Finkelstein,[‡] and Ivan Borzenets^{*,†}

[†]*Department of Physics and Astronomy, Texas A&M University, College Station, 77843, Texas, USA*

[‡]*Department of Physics, Duke University, Durham, 27701, North Carolina, USA*

[¶]*Department of Physics and Astronomy, Purdue University, West Lafayette, 47907, Indiana, USA*

[§]*Advanced Materials Laboratory, NIMS, Tsukuba, 305-0044, Japan*

E-mail: borzenets@tamu.edu

Abstract

We perform transport measurements on proximitized, ballistic, bilayer graphene Josephson junctions (BGJJs) in the intermediate-to-long junction regime ($L > \xi$). We measure the device's differential resistance as a function of bias current and gate voltage for a range of different temperatures. The extracted critical current I_C follows an exponential trend with temperature: $\exp(-k_B T/\delta E)$. Here $\delta E = \hbar v_F/2\pi L$: an expected trend for intermediate-to-long junctions. From δE , we determine the Fermi velocity of the bilayer graphene, which is found to increase with gate voltage. Simultaneously, we show the carrier density dependence of δE , which is attributed to the quadratic dispersion of bilayer graphene. This is in contrast to single layer graphene Josephson

junctions, where δE and the Fermi velocity are independent of the carrier density. The carrier density dependence in BGJJs allows for additional tuning parameters in graphene-based Josephson Junction devices.

Keywords

Graphene, Bilayer Graphene, Josephson Junctions, Fermi Velocity, Andreev Levels.

Ballistic graphene Josephson junctions (GJJs) have been widely utilized as a platform to study novel quantum physics phenomena^{1,2} and devices,³ including: entangled pair generation,^{4,5} topological states arising from the mixing of superconductivity and quantum Hall states,⁶ as well as photon sensing via bolometry/calorimetry.⁷ Superconductor-normal metal-superconductor Josephson junction (SNSJJ) hosts Andreev bound states (ABS), which carry supercurrents across the normal region of the JJ; in order to enter the ballistic regime, a disorder-free weak link and high transparency at the SN interface are necessary. Hexagonal Boron-Nitride (hBN) encapsulated graphene as a weak link enables highly transparent contacts at the interface whilst keeping graphene clean throughout the fabrication process.⁸ Here, we study proximitized, ballistic, bilayer graphene Josephson junctions (BGJJs). Bilayer graphene devices (in contrast to monolayer) allow extra potential tunability via a non-linear dispersion relation, applied displacement field, or lattice rotation.¹

The critical current (I_C) of SNSJJ in the intermediate-to-long regime, where the junction length (L) \geq superconducting coherence length (ξ_0), scales with temperature (T) as $I_C = \exp(-k_B T / \delta E)$. Here, $\delta E = \hbar \nu_F / 2\pi L$, an energy scale related to the ABS level spacing.^{2,9-13} Note that in the intermediate regime ($L \approx \xi_0$) δE is found to be suppressed.⁵ A previous study of GJJs found that in this regime, the relation is held more precisely when ξ was taken into account along with L , that is: $\delta E = \hbar \nu_F / 2\pi(L + \xi)$.^{2,13} Monolayer graphene displays a linear dispersion relation, which results in a constant fermi velocity (ν_{F0}). Thus, in ballistic GJJs, δE remains independent of the carrier density. In comparison, bilayer graphene displays a quadratic dispersion relation at low energies. In BGJJs we studied, a

back-gate voltage (V_G) controls the carrier density; and δE dependence on V_G is observed. Using δE , we extract the Fermi velocity in bilayer graphene: It is seen that ν_F increases with V_G , and saturates to the constant value, ν_{F0} , of the monolayer graphene.

Our device consists of a series of four terminal Josephson junctions (on SiO_2/Si substrate) made with hBN encapsulated bilayer graphene contacted by Molybdenum-Rhenium (MoRe) electrodes. Bilayer graphene is obtained via the standard exfoliation method. It is then encapsulated in hexagonal Boron-Nitride using the dry transfer method.¹⁴ MoRe of 80 nm thickness is deposited via DC magnetron sputtering. The resulting device has four junctions of lengths 400 nm, 500 nm, 600 nm, and 700 nm. The width of the junctions is 4 μm . The device is cooled in a Leiden cryogenics dilution refrigerator operated at temperatures above 1 K, and measurements were performed using the standard four-probe lock-in method. A gate voltage V_G is applied to the Si substrate with the oxide layer acting as a dielectric, which allows modulation of the carrier density.^{2,5,6,15-17} Figure. 1(a) displays the differential

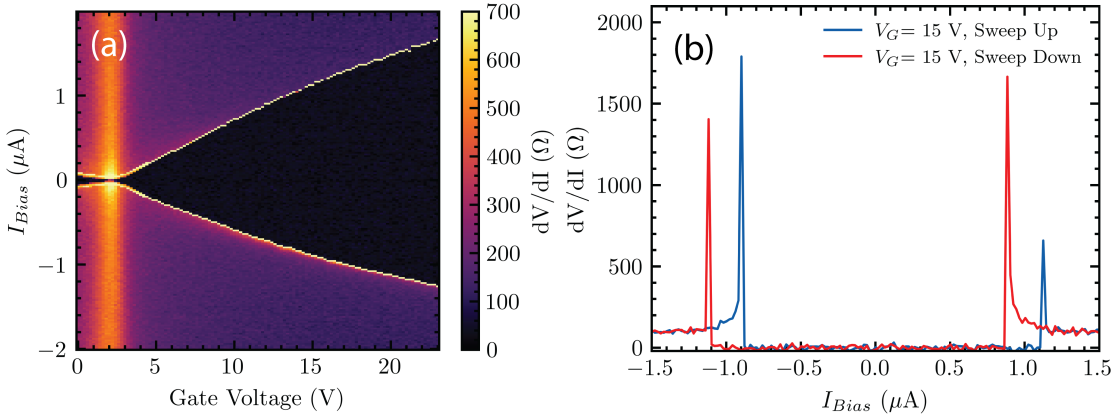


Figure 1: (a) Differential resistance (dV/dI) versus gate voltage (V_G) and bias current I_{Bias} taken at $T = 1.37$ K. The black region around zero bias corresponds to the superconducting state. I_{Bias} is swept up (from negative to positive). Thus, the transition at negative bias corresponds to the re-trapping current I_R , while the transition at positive bias is the switching current I_C . (b) Vertical line cut of the resistance map taken at $V_G = 15$ V, $T = 1.37$ K, showing device's dV/dI versus bias current. Blue line corresponds to I_{Bias} swept up, with red line swept down (positive to negative).

resistance (dV/dI) map of the 400 nm junction at $T = 1.37$ K; we see zero resistance (black region) across all applied V_G indicating the presence of supercurrent. As the bias current

I_{bias} is swept from negative to positive values, the junction first reaches its superconducting state at a value $|I_{bias}| = I_R$, known as the re-trapping current. Then, as $|I_{bias}|$ is increased to higher positive values, the junction transitions to the normal state at $|I_{bias}| = I_S$, known as the switching current. Figure. 1(a) shows that the junction can sustain a larger region of critical current as we modulate the carrier density to higher values via V_G . Fig. 1(b) displays line traces extracted from the dV/dI map which shows hysteresis in I_R and I_S . This is a commonly observed phenomenon in underdamped junctions,^{15,18} or can also be attributed to self-heating.^{16,17,19} The measured switching current I_S is slightly suppressed compared to the junction's "true" critical current I_C . However, previous measurements on the statistical distribution of I_S in similar graphene devices found that I_S is suppressed from I_C by no more than 10% for critical currents up to a few μA .^{2,20-22}

Extracting the critical current I_C from the differential maps for different temperatures, we can see that I_C falls exponentially with inverse T (Figure. 2c) We also extract the conductance of the junction in the normal regime ($I_{Bias} \gg I_C$). Figure. 2(b) shows this conductance (G) for the 400 nm junction device. Due to the significant contact resistance (R_C) of the device, the measured conductance G is uniformly suppressed compared to the ballistic limit expectation. However, when accounting for R_C within the fit, we find that the conductance G scales as the square-root (as opposed to linearly) of V_G (blue curve of Figure 2(b)). This is consistent with ballistic transport.^{2,23} To further demonstrate the ballistic nature of the device, we present normal resistances (R_N) of junctions of length 500 nm, 600 nm, and 700 nm with the fitted, constant contact resistance R_C subtracted (Figure. 2(b) inset). The inset plot shows that the values of $R_N - R_C$ are independent of the junction length, demonstrating the ballistic nature of the devices.

To extract δE of the junction, we go to the discussion of I_C vs. the temperature trends in Figure. 2(c). Here, the y-axis is plotted in logarithmic scale. From the slope of the curves $\text{Log}(I_C) = -(k_B/\delta E)T$ for each gate, one can extract δE versus V_G (plotted in Figure. 3a). Unlike for the case of monolayer graphene, a clear dependence on V_G is seen (The observed

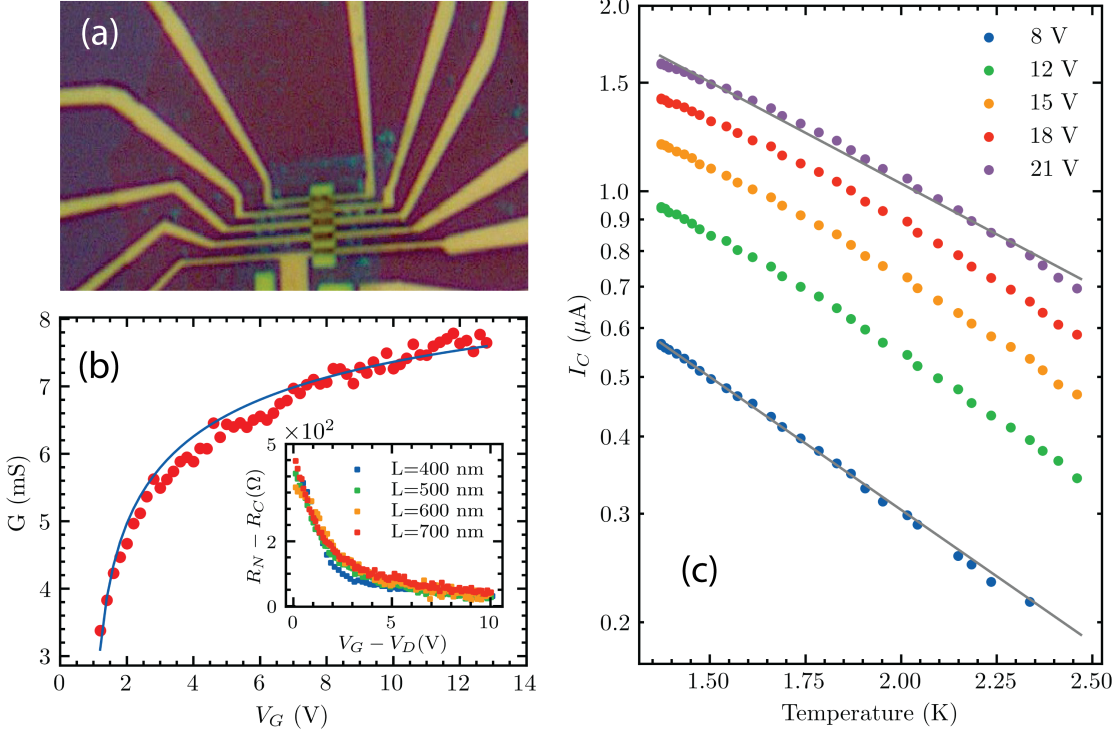


Figure 2: (a) Device picture. Image shows series of junctions with different Lengths: 400 nm, 500 nm, 600 nm and 700 nm. (b) The ballistic conductance vs Gate voltage for $L = 400$ nm junction. The blue curve corresponds to the fit for ballistic devices, with an addition of a contact resistance. The inset shows junction resistance minus the parasitic contact resistance plotted against gate voltage from the Dirac point for all our devices. (c) Critical currents I_C of $L = 400$ nm junction plotted against temperature T , for various gate voltages, on a semi-log scale. The plots show V_G dependence of I_C : the gray lines show that the slope of the curve for the lowest plotted gate $V_G = 8$ V, is smaller than the slope of the highest plotted gate $V_G = 21$ V.

trend further supports the view that our devices operate in the long ballistic regime. Diffusive Josephson junctions are governed by the Thouless energy $E_{Th} \propto 1/[(R_N - R_C)\sqrt{V_G - V_D}]^{22,24}$ which does not match the trend with respect to V_G seen in Figure. 3(a)). The energy δE scales linearly with the Fermi velocity v_F (Figure. 3(b)). Note that calculating v_F from δE for junctions in the intermediate regime requires knowledge of the superconducting coherence length ξ . In the fit discussed below, we use ξ 's dependence in v_F .

We now compare the experimentally obtained δE (and v_F) to the theoretical expectation. With the dispersion relation for bilayer graphene written as : $\mathcal{E} = \frac{1}{2}\gamma_1(\sqrt{1 + 2\hbar^2k^2/\gamma_1^2m^*} - 1)$, we get the expression for the Fermi velocity : $v_F = \sqrt{\frac{2\mathcal{E}_F\gamma_1(\mathcal{E}_F + \gamma_1)}{(2\mathcal{E}_F + \gamma_1)^2m^*}}$.²⁵⁻²⁷ Here, $\gamma_1 = 0.39$ eV

a parameter describing the interlayer coupling,²⁵ k is the momentum wavevector, m^* is the effective mass of electrons. Moreover, the Fermi energy \mathcal{E}_F for bilayer graphene scales as: $\mathcal{E}_F = \frac{\hbar^2 \pi |n|}{2m^*}$. The carrier concentration n , controlled by the applied gate voltage V_G , is given by $n = \frac{V_G - V_D}{e} C_{Total}$ with V_D as the gate voltage at the Dirac point. The total capacitance C_{Total} is a combination of quantum capacitance C_q and gate oxide capacitance C_{ox} : $C_{Total} = \left[\frac{1}{C_{ox}} + \frac{1}{C_q} \right]^{-1}$. The quantum capacitance C_q for bilayer graphene is determined by $C_q = \frac{2e^2 m^*}{\pi \hbar^2}$, where e is the electron charge. The gate oxide capacitance per unit area is $C_{ox} = \frac{\epsilon_0 \epsilon_r}{d}$, where ϵ_0 is the vacuum permittivity, ϵ_r is the relative permittivity of the oxide, and d is the thickness of the oxide layer. For silicon oxide gate with $d = 300$ nm we get $C_{ox} \approx 115 \mu F/m^2$. Thus, the full expression for the Fermi velocity v_F is:

$$v_F = \hbar \sqrt{\frac{2\pi e \epsilon_0 \epsilon_r \gamma_1 (V_G - V_D) (2de^2 \gamma_1 m^* + \pi \epsilon_0 \epsilon_r \hbar^2 (e(V_G - V_D) + \gamma_1))}{m^* (2de^2 \gamma_1 m^* + \pi \epsilon_0 \epsilon_r \hbar^2 (2e(V_G - V_D) + \gamma_1))^2}} \quad (1)$$

Note that the effective mass m^* typically ranges from $0.024 m_e$ to $0.058 m_e$ for $1 * 10^{12} \sim 4 * 10^{12}$ carriers/cm²,²⁸ where m_e is the electron rest mass. Experimental data provides us with the following: $\delta E(V_G) = \frac{\hbar}{2\pi(L+\xi)} v_F$. We also note that ξ has a dependence on v_F and the superconducting gap Δ : $\xi = \hbar v_F / 2\Delta$.¹³ To fit δE , the model is set as: $\delta E(V_G) = \mathcal{F}(m^*, \Delta, V_D, d)$ where m^*, Δ, V_D, d are the fitting parameters, and V_G is the independent variable. (We use the as-designed length of the device L , and take $\epsilon_r = 3.9$ for SiO_2 .)

Table 1: The fitting parameters used to match the measured δE , and consequently the Fermi velocity v_F , versus gate to the theoretical expectation described in Equation 1. We see that resulting fitted values match closely to what is expected. The expected gate dielectric thickness d is estimated from the substrate specifications plus the bottom hBN thickness. The expected Dirac point voltage V_D is obtained from the resistance map. The expectations for superconducting gap Δ and the effective mass m_i are obtained from previous works.^{5,28}

Parameter	Fitted Value	Expected Value
Δ	0.99 meV	$0.8 \sim 1.2$ meV
d	323 nm	$280 \sim 330$ nm
m^*	$0.028 m_e$	$0.02 \sim 0.06 m_e$
V_D	2.04 V	$\approx +2$ V

The resulting fits of the data from the 400 nm junction for δE and v_F are plotted as solid lines in Figure. 3(a) and Figure. 3(b) respectively. Moreover, taking the fitted parameters from Table 1, we calculate the Fermi velocity v_F for the available data points of all other junctions on the same substrate. As seen from Figure. 3(b), the calculated v_F of all devices is in good agreement with the fit obtained from the 400 nm junction (This is as expected for devices on the same substrate; as long as they have consistent parasitic doping and superconductor-graphene contact interface). The fitted parameters are summarized in Table 1. All fall within the range of expected values, with Δ being consistent with previously measured values for graphene/MoRe junctions.² Furthermore, using the values obtained from the model, we find that v_F saturates to the value of $1.1 * 10^6$ m/s as V_G tends to infinity.

In conclusion, we study the evolution of the critical current with respect to the gate in bilayer graphene Josephson Junctions (BGJJs). Using the critical current-temperature relation expected for intermediate-to-long junctions, we extract the relevant energy scale δE and find that it has a clear gate dependence. As δE is proportional to the Fermi velocity v_F in bilayer graphene, we are able to match the observed gate dependence to the theoretical expectation. Our observation is contrasted with monolayer graphene JJs, which do not have a gate-dependent δE . This result showcases the greater tunability of BGJJs, and offers additional avenues for device characterization. Although not observed here, it should be possible to engineer Josephson junctions that transition from the short to the intermediate/long ballistic regimes in-situ via gate voltage. The ability to tune ABS level spacing could have applications in self-calibrating sensors, or for matching resonance conditions in multi-terminal superconducting devices.

L.R. acknowledges support from NSF (DMR-2005092 award) for contact depositon. G.F. acknowledges support from Duke University. I.V.B. and A.S. acknowledge the support from Texas A&M University.

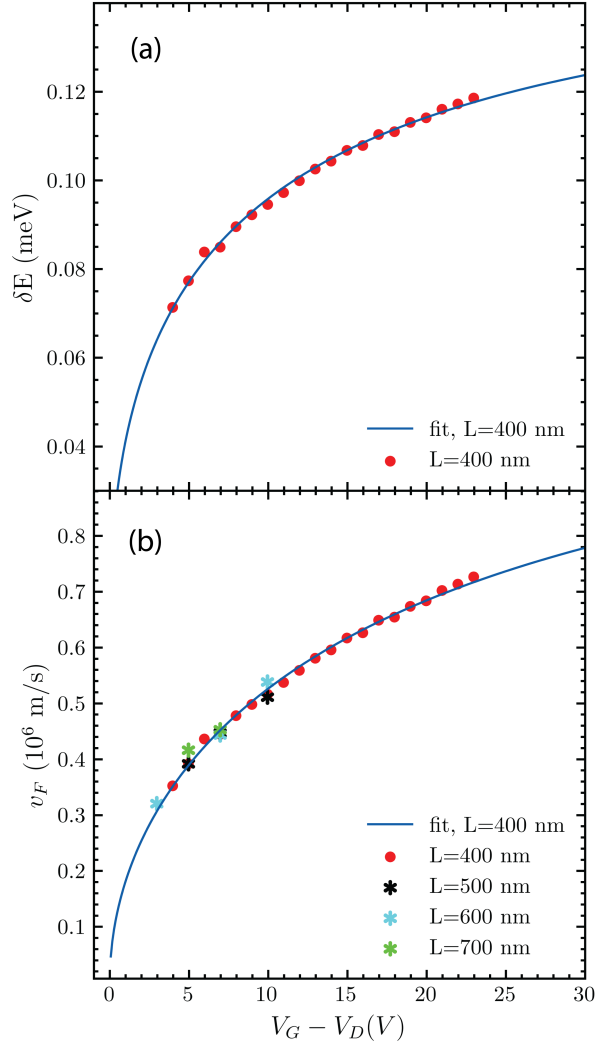


Figure 3: (a) Energy δE extracted from the slope of $\log(I_C)$ vs T plotted against the gate voltage V_G from the Dirac point of the junction with $L = 400$ nm. We see δE dependence on the carrier density modulated via the gate voltage for the junction. (b) Fermi velocity (v_F) calculated from δE using the device dimensions, and parameters obtained from the fit to theory. The solid line represents the theoretical trend as fitted to the data for the $L = 400$ nm junction. In addition, panel (b) shows calculated v_F for the other junctions using parameters obtained from the $L = 400$ nm fit.

References

(1) Park, G. H.; Lee, W.; Park, S.; Watanabe, K.; Taniguchi, T.; Cho, G. Y.; Lee, G. H. Controllable Andreev Bound States in Bilayer Graphene Josephson Junctions from Short to Long Junction Limits. *Physical Review Letters* **2024**, *132*.

(2) Borzenets, I. V.; Amet, F.; Ke, C. T.; Draelos, A. W.; Wei, M. T.; Seredinski, A.; Watanabe, K.; Taniguchi, T.; Bomze, Y.; Yamamoto, M.; Tarucha, S.; Finkelstein, G. Ballistic Graphene Josephson Junctions from the Short to the Long Junction Regimes. *Phys. Rev. Lett.* **2016**, *117*, 237002.

(3) Kroll, J. G.; Uilhoorn, W.; van der Enden, K. L.; de Jong, D.; Watanabe, K.; Taniguchi, T.; Goswami, S.; Cassidy, M. C.; Kouwenhoven, L. P. Magnetic field compatible circuit quantum electrodynamics with graphene Josephson junctions. *Nature Communications* **2018**, *9*.

(4) Chen, W.; Shi, D. N.; Xing, D. Y. Long-range Cooper pair splitter with high entanglement production rate. *Scientific Reports* **2015**, *5*.

(5) Borzenets, I. V.; Shimazaki, Y.; Jones, G. F.; Craciun, M. F.; Russo, S.; Yamamoto, M.; Tarucha, S. High Efficiency CVD Graphene-lead (Pb) Cooper Pair Splitter. *Scientific Reports* **2016**, *6*.

(6) Amet, F.; Ke, C. T.; Borzenets, I. V.; Wang, J.; Watanabe, K.; Taniguchi, T.; Deacon, R. S.; Yamamoto, M.; Bomze, Y.; Tarucha, S.; Finkelstein, G. Supercurrent in the quantum Hall regime. *Science* **2016**, *352*, 966–969.

(7) Lee, G.-H.; Efetov, D. K.; Jung, W.; Ranzani, L.; Walsh, E. D.; Ohki, T. A.; Taniguchi, T.; Watanabe, K.; Kim, P.; Englund, D.; Fong, K. C. Graphene-based Josephson junction microwave bolometer. *Nature* **2020**, *586*, 42–46.

(8) Dean, C. R.; Young, A. F.; Meric, I.; Lee, C.; Wang, L.; Sorgenfrei, S.; Watanabe, K.; Taniguchi, T.; Kim, P.; Shepard, K. L.; Hone, J. Boron nitride substrates for high-quality graphene electronics. *Nature Nanotechnology* **2010**, *5*, 722–726.

(9) Kulik, I. O. Macroscopic Quantization and the Proximity Effect in S-N-S Junctions. *Soviet Physics JETP* **1970**, *30*, 944.

(10) Bardeen, J.; Johnson, J. L. Josephson Current Flow in Pure Superconducting-Normal-Superconducting Junctions. *Physical Review B* **1972**, *5*, 72–78.

(11) Svidzinsky, A. V.; Antsygina, T. N.; Bratus, E. N. Superconducting current in wide sns junctions. *Soviet Physics JETP* **1972**, *34*, 860.

(12) Svidzinsky, A. V.; Antsygina, T. N.; Bratus, E. N. Concerning the theory of the Josephson effect in pureSNS junctions. *Journal of low Temperature Physics* **1973**, *10*, 131–136.

(13) Bagwell, P. F. Suppression of the Josephson current through a narrow, mesoscopic, semiconductor channel by a single impurity. *Phys. Rev. B* **1992**, *46*, 12573–12586.

(14) Wang, L.; Meric, I.; Huang, P. Y.; Gao, Q.; Gao, Y.; Tran, H.; Taniguchi, T.; Watanabe, K.; Campos, L. M.; Muller, D. A.; Guo, J.; Kim, P.; Hone, J.; Shepard, K. L.; Dean, C. R. One-Dimensional Electrical Contact to a Two-Dimensional Material. *Science* **2013**, *342*, 614–617.

(15) Borzenets, I. V.; Coskun, U. C.; Jones, S. J.; Finkelstein, G. Phase Diffusion in Graphene-Based Josephson Junctions. *Physical Review Letters* **2011**, *107*.

(16) Borzenets, I. V.; Coskun, U. C.; Mebrahtu, H. T.; Bomze, Y. V.; Smirnov, A. I.; Finkelstein, G. Phonon Bottleneck in Graphene-Based Josephson Junctions at Millikelvin Temperatures. *Physical Review Letters* **2013**, *111*.

(17) Tang, J.; Wei, M. T.; Sharma, A.; Arnault, E. G.; Seredinski, A.; Mehta, Y.; Watanabe, K.; Taniguchi, T.; Amet, F.; Borzenets, I. Overdamped phase diffusion in hBN encapsulated graphene Josephson junctions. *Phys. Rev. Research* **2022**, *4*, 023203.

(18) Tinkham, M. *Introduction to Superconductivity*; Dover Publications, 2004.

(19) Courtois, H.; Meschke, M.; Peltonen, J. T.; Pekola, J. P. Origin of Hysteresis in a Proximity Josephson Junction. *Physical Review Letters* **2008**, *101*.

(20) Coskun, U. C.; Brenner, M.; Hymel, T.; Vakaryuk, V.; Levchenko, A.; Bezryadin, A. Distribution of Supercurrent Switching in Graphene under the Proximity Effect. *Physical Review Letters* **2012**, *108*.

(21) Lee, G. H.; Jeong, D.; Choi, J. H.; Doh, Y. J.; Lee, H. J. Electrically Tunable Macroscopic Quantum Tunneling in a Graphene-Based Josephson Junction. *Physical Review Letters* **2011**, *107*.

(22) Ke, C. T.; Borzenets, I. V.; Draelos, A. W.; Amet, F.; Bomze, Y.; Jones, G.; Craciun, M.; Russo, S.; Yamamoto, M.; Tarucha, S.; Finkelstein, G. Critical Current Scaling in Long Diffusive Graphene-Based Josephson Junctions. *Nano Letters* **2016**, *16*, 4788–4791.

(23) Castro Neto, A. H.; Guinea, F.; Peres, N. M. R.; Novoselov, K. S.; Geim, A. K. The electronic properties of graphene. *Rev. Mod. Phys.* **2009**, *81*, 109–162.

(24) Dubos, P.; Courtois, H.; Pannetier, B.; Wilhelm, F. K.; Zaikin, A. D.; Schön, G. Josephson critical current in a long mesoscopic S-N-S junction. *Phys. Rev. B* **2001**, *63*, 064502.

(25) McCann, E.; Koshino, M. The electronic properties of bilayer graphene. *Reports on Progress in Physics* **2013**, *76*, 056503.

(26) Fang, T.; Konar, A.; Xing, H.; Jena, D. Carrier statistics and quantum capacitance of graphene sheets and ribbons. *Applied Physics Letters* **2007**, *91*.

(27) Fates, R.; Bouridah, H.; Raskin, J. P. Probing carrier concentration in gated single, bi- and tri-layer CVD graphene using Raman spectroscopy. *Carbon* **2019**, *149*, 390–399.

(28) Zou, K.; Hong, X.; Zhu, J. Effective mass of electrons and holes in bilayer graphene: Electron-hole asymmetry and electron-electron interaction. *Physical Review B* **2011**, *84*.